# Chapter 6
# ELECTRONIC STRUCTURE AND OPTICAL STUDY OF Mn-DOPED $Er_2Ti_2O_7$

## 6.1 Introduction

After studying the low-temperature magnetic properties of and the role of the Mn substitution at the Ti site on spin dynamics of an Ising and XY type pyrochlore compound, i.e., $Dy_2Ti_2O_7$ and $Er_2Ti_2O_7$. The optical and electronic studies of Mn-substituted $Dy_2Ti_2O_7$ have already been discussed in Chapter 4. This chapter deals with a similar study of a different class of XY-type pyrochlore system, i.e., $Er_2Ti_2O_7$.

The energy levels of the substituted ion (i.e., $Mn^{4+}$ having $3d^3$ electronic configuration) influenced by a crystal field of arbitrary symmetry is represented by eigenvalues of the given crystal field (C.F.) Hamiltonian: $H = \sum_{p=2,4}\sum_{k=-p}^{p} B_p^k O_p^k$, Where $O_p^k$ are the linear combinations of the irreducible tensor operators acting on the angular part of the $Mn^{4+}$ ion wave functions and $B_p^k$ are the C.F. parameters proportional to the wave function overlap between the ligand atom and the central rare earth ion [51]. These terms incorporate the structural and geometrical information of the host lattice and the crystallographic arrangement of the host lattice atoms and ions around the $Mn^{4+}$ ion. In this compound, the $Mn^{4+}$ ion substitutes for the tetravalent $Ti^{4+}$ that occurs in a sixfold coordination of oxygen ions (trigonal antiprism). The lattice deformations are minimized since no charge-compensating

mechanisms are needed in this case. Mn can assume many oxidation states, such as 2+, 3+, 4+, and 5+, depending on the chemical environment of the Mn ion. Mn ion usually assumes the 4+ oxidation state when located on an octahedral site in solids because the octahedral crystal field creates a large energy gap between the occupied $t_{2g}$ and the empty $e_g$ orbitals in $Mn^{4+}$. The emission spectra for $Mn^{4+}$ show a sharp line corresponding to $2E_g$ to $4A_{2g}$ transition and is associated with a spin-flip between the low spin and high spin state [150]. In particular, perturbation through substitution is an effective way to alter the band gap. It strongly influences the electronic structure by introducing new charge carriers or heightening orbital overlap between the transition metal and oxygen atoms. It flexibly modifies the electrical band structure near the Fermi level.

In this study, structural distortion was induced, and different multiplets of $Er_2Ti_{2-x}M_xO_7$ (x = 0.00, 0.10, & 0.20) series were studied. Initially, we start with ab initio calculation using DFT to study the electronic structure of the Valence Band (V.B.) and Conduction Band (C.B.), Band gap energy ($E_g$), orbitals involved in hybridization and DOS for the system. Further local electronic correlation effects and electronic structure for $Er_2Ti_{2-x}M_xO_7$ were studied through Raman and XPS experiments. Raman spectroscopy is sensitive to detecting local bonding distance and bonding angle. XPS technique is based on the excitation of electrons from deeply bound core levels to unoccupied levels. Optical characterization tools in the visible and infrared regions using UV-visible (220-1400 nm) and photoluminescence (PL) spectroscopic techniques have been used to study the transition states. The spectroscopic studies of $Er_2Ti_2O_7$ with subsequent perturbation through Mn inclusion in its matrix have been taken up. This study attempts to appraise the relationship between the structural, optical, and electronic properties of the $Er_2Ti_{2-x}M_xO_7$ series to bridge the knowledge gap described below.

### 6.1.1 Theoretical calculation of electronic structure using density functional theory (DFT) calculations

The electronic structure (band and DOS) has been calculated using density functional theory to theoretically study the role of Mn on the electronic structure of $Dy_2Ti_2O_7$. **Figure 6.1(b)** presents the partial density of states (PDOSs) and total density of states of $Er_2Ti_2O_7$ using local density approximation (LDA) approximation**.** PDOSs indicate that the major contribution of valence states comes from the hybridization of O-2p state with Er-6s, Er-5d and Ti-3d states. O-2p, Er-6s, and O-2s states prominently contribute to the formation of lower-lying valence states, while the conduction band is majorly formed through the hybridization of Er-5d states and Ti-3d states. From the total density of states (DOS) calculation using LDA approximation, the calculated bandgap of $Er_2Ti_2O_7$ comes out to be 2.90 eV, which is shown in **Figure 6.1(a)**. The same calculation, i.e., total DOS using LDA-1/2 approximation that considers the self-energy correction, is shown in **Figure 6.1 (d)** [121]. A much closer value of the band gap for such type of system is obtained if we consider self-energy potential focused at the anion site that nullifies the energy related to electron-hole recombination. This approximation gives 4.06 eV as the band gap value which is closer to the experimental band gap value of 3.84 eV calculated using Tauc plot. The band structure is shown in **Figure 6.1(c)**, which specifies gamma points to be the maxima and minima for the valence band and conduction band, respectively. It indicates that $Er_2Ti_2O_7$ exhibits direct type of band gap transition manifested via both LDA and LDA-1/2 methods.

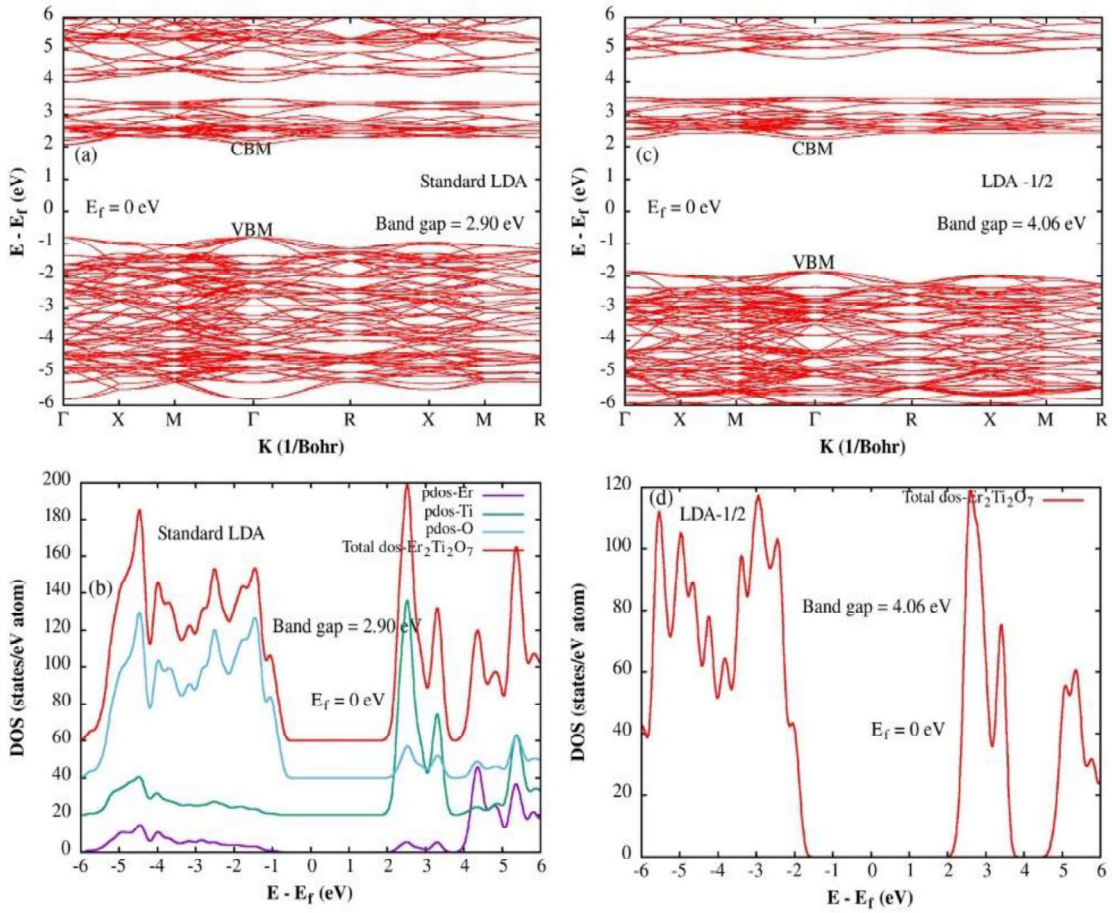


**Figure 6.1 Calculated (a) band Structure, and (b) total density of state along with partial density of states for $Er_2Ti_2O_7$ using LDA. Calculated (c) band Structure and (d) total density of state for $Er_2Ti_2O_7$ using LDA -1/2.**

Next, the role of Mn inclusion at titanium site was studied in context to the variations in the values of the band gap. For x = 0.10, i.e., five percent Mn inclusion causes the emergence of a new state of Mn above and below the Fermi level. This is depicted in **Figure 6.2(b),** which shows the total and partial density of states through LDA approximation. The same approximation gives the band gap value of this system to be 2.05 eV.

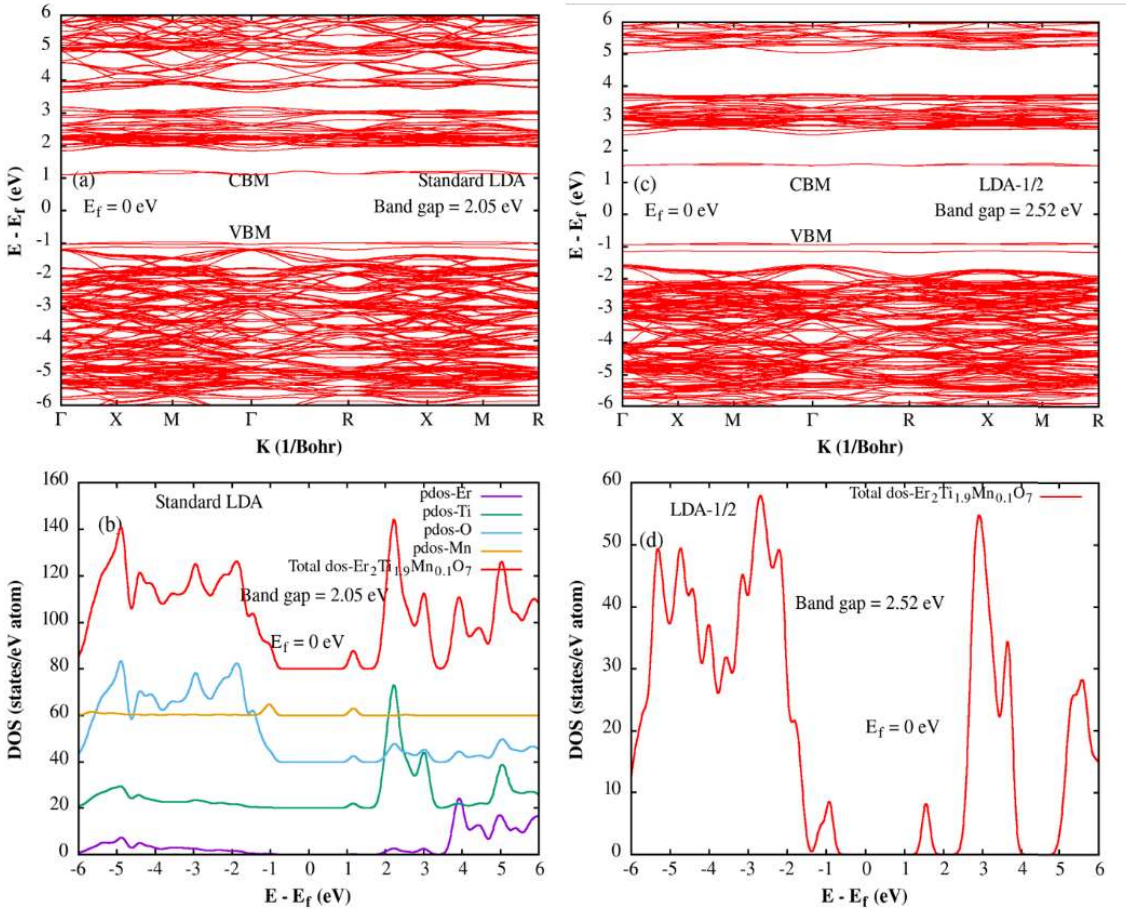


**Figure 6.2 Calculated (a) band structure and (b) total density of state along with partial density of states for $Er_2Ti_{1.9}Mn_{0.1}O_7$ using LDA. Calculated (c) band Structure and (d) total density of state for $Er_2Ti_{1.9}Mn_{0.1}O_7$ using LDA -1/2.**

Orbitals hybridized for conduction and valence band formation are similar to that of $Er_2Ti_2O_7$ along with the involvement of $Mn^{4+}$ 3d state too. In Mn deployed systems, charge transfer phenomenon takes place between Mn-3d states ($Mn^{3+}$) and O-2p ligand states, which is linked with the C.B. and V.B. formation due to the spin-flip between the low and high spin state. The band structure for this system is shown in **Figure 6.2(a),** which indicates gamma point as the high symmetry point involved in the direct transition. Next, the total density of state for this system using LDA-1/2 approximation is shown in **Figure 6.2(d).** It shows that the same orbitals are involved in hybridization for band formation, only the additional emergence of a small cross-section near the conduction band edge leads to the decrease in the experimental bandgap from 4.06 eV (x = 0) to 2.52 eV (x = 0.1) with Mn inclusion. **Figure 6.2(c)** shows the band structure (x = 0.1) along with the high symmetry Gamma point associated in direct bandgap transition.

**Figure 6.3(b)** shows the Partial density of states (x = 0.2) through LDA method. The cross section of oxygen 2p state and Mn-d state increases near the Fermi level with an increase in the doping percentage of Mn at Ti site in $Er_2Ti_2O_7$. Er-5d and Ti-3d states also contribute to hybridization in conduction and valence band formation along with O-2p and Mn -3d. For x = 0.2, both band structure and total density of state results in the theoretically obtained bandgap value of 1.85 eV which is shown in **Figure 6.3(a)** and **Figure 6.3(b)** respectively. For the same system, band gap is 2.41 eV when self-energy correction is considered in LDA-1/2 approximation. **Figure 6.3(c) and (d)** show the band structure and total density of states for x = 0.2.

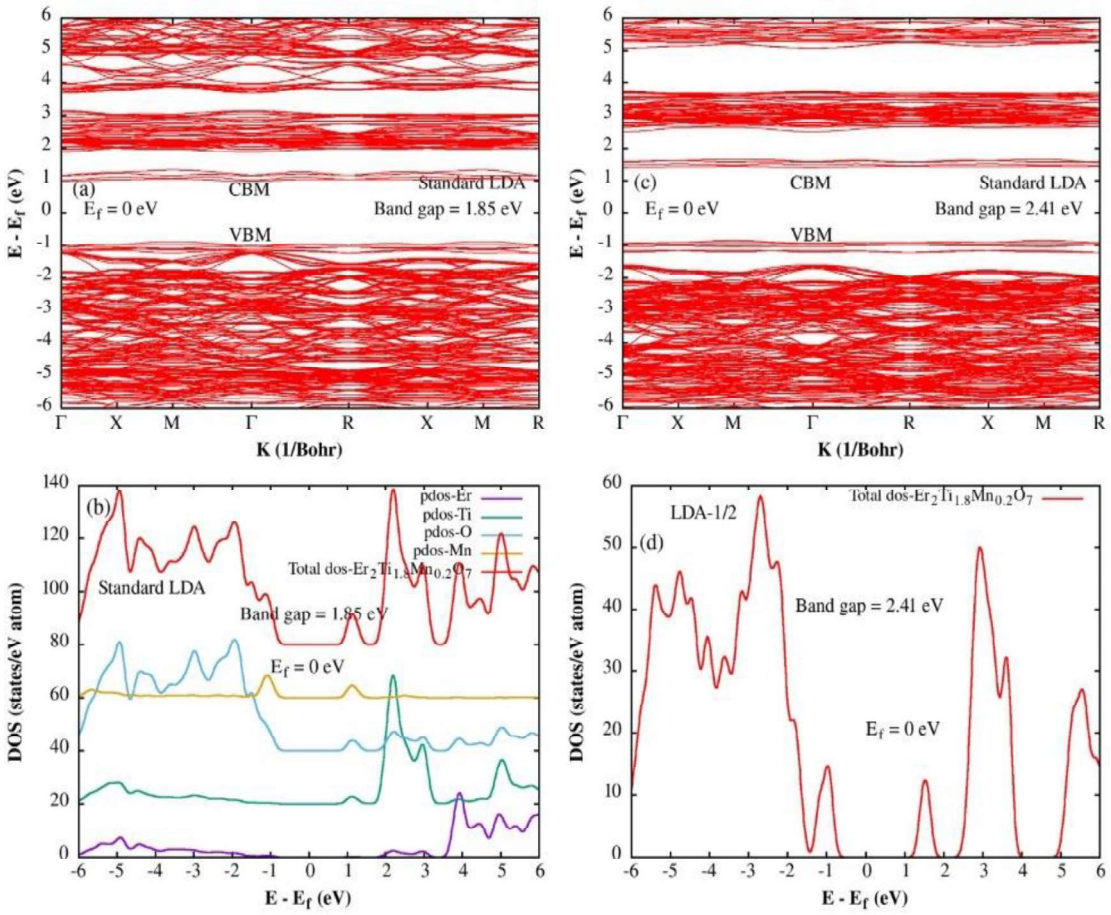


**Figure 6.3 Calculated (a) band Structure, and (b) total density of state along with partial density of states for $Er_2Ti_{1.8}Mn_{0.2}O_7$ using LDA. Calculated (c) band Structure and (d) total density of state for $Er_2Ti_{1.8}Mn_{0.2}O_7$ using LDA - 1/2.**

### 6.1.2 Raman spectroscopy

Raman spectroscopy is sensitive to detecting local bonding distance and bonding angle [123]. The effect of Mn inclusion on phonon behavior in the $Er_2Ti_2O_7$ matrix has been studied using room temperature Raman measurement, performed with an excitation wavelength of 532 nm.

Raman spectra for the $Er_2Ti_{2-x}Mn_xO_7$ sample were recorded in the wave number range of (150 – 850) $cm^{-1,}$ as shown in **Figure 6.4.**

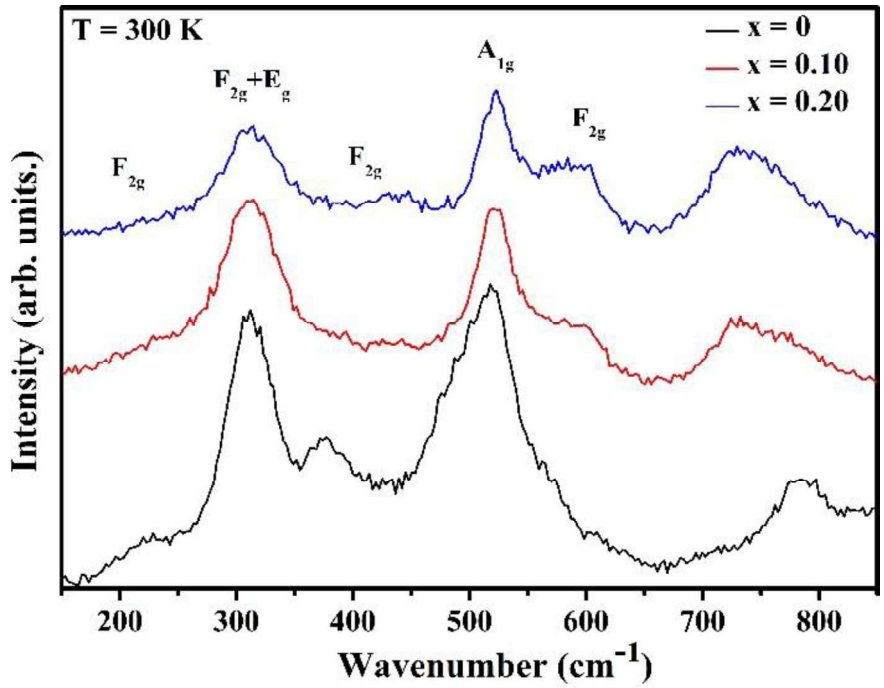


**Figure 6.4 Room temperature Raman spectra for $Er_2Ti_{2-x}Mn_xO_7$ (x = 0, 0.05, 0.10, 0.15, 0.20) showing the presence of Raman modes corresponding to pyrochlore structure**

Since $Er_2Ti_2O_7$ belongs to the cubic- $Fd\bar{3}m$ structural symmetry, where Z = 8, for the cubic pyrochlores, the corresponding factor group is $O_h$. The site symmetry for A and B cations is $D_{3d}$, and for O(1) and O(2) anion is $C_{2v}$ and $T_d$, respectively. Group theory predicts six Raman active modes. The irreducible representation for six Raman active modes is $\Gamma_R = A_{1g} + E_g + 4F_{2g}$. These Raman active modes involve only the motion of oxygen atoms. Here, one $F_{2g}$ mode is associated with 8b oxygen, while the other three $F_{2g}$ modes are related to 48f oxygen [126]–[129]. The Raman spectra for $Er_2Ti_2O_7$ as shown in **Figure 6.4.** exhibit two bands with

a strong intensity. The Raman spectra depicted in **Figure 6.4** show the six Raman active modes**.** Hence, it is obvious that all the samples own cubic pyrochlore structures. The most prominent band, cantered at 516 $cm^{-1}$, is $A_{1g}$. $A_{1g}$ is related to the stretching of Ti-O bonds and the bending of O-Ti-O angles in the $TiO_6$ octahedra of the $Er_2Ti_2O_7$ system. The second band, cantered at 311 $cm^{-1}$, is attributed to two modes ($F_{2g}$ and $E_g$) with very close wavenumbers [122], [123]. The intensity of the peaks at 311 $cm^{-1}$ and 516 $cm^{-1}$ decreases with a progressive increase in Mn concentration. The variations in peak intensity can be attributed to alterations in the local crystal field and symmetry of the system caused by the Mn substitution. The broadening of the peak at 311 $cm^{-1}$ with increasing Mn concentration suggests local disordering Mn substitution Raman-active modes involving the movement of oxygen atoms are due to Er−O stretching, O−Er−O bending, O−O stretching, and O−Ti−O bending and stretching [123].

### 6.1.3 XPS spectroscopy

The survey scan confirmed that all constituent elements were present in the compound. Further, all peaks in the spectra are assigned their electronic states as per the binding energy obtained from the XPS data book [131]. Except for the presence of C-1s peak at 284.5 eV in the form of impurity being absorbed from the air, all the identified peaks belong to Er, Ti, and O states for the $Er_2Ti_2O_7$ system. This surface-absorbed/adsorbed carbon has been found in many systems but does not affect its physical properties. The survey scan of $Er_2Ti_2O_7$ presents the KLL Auger oxygen peak at 779.4 and 794.3 eV, as shown in **Figure 6.5.** The Auger feature disappears with Mn inclusion for both x = 0.1 and 0.2 [**Figure 6.6** and **Figure 6.7**].

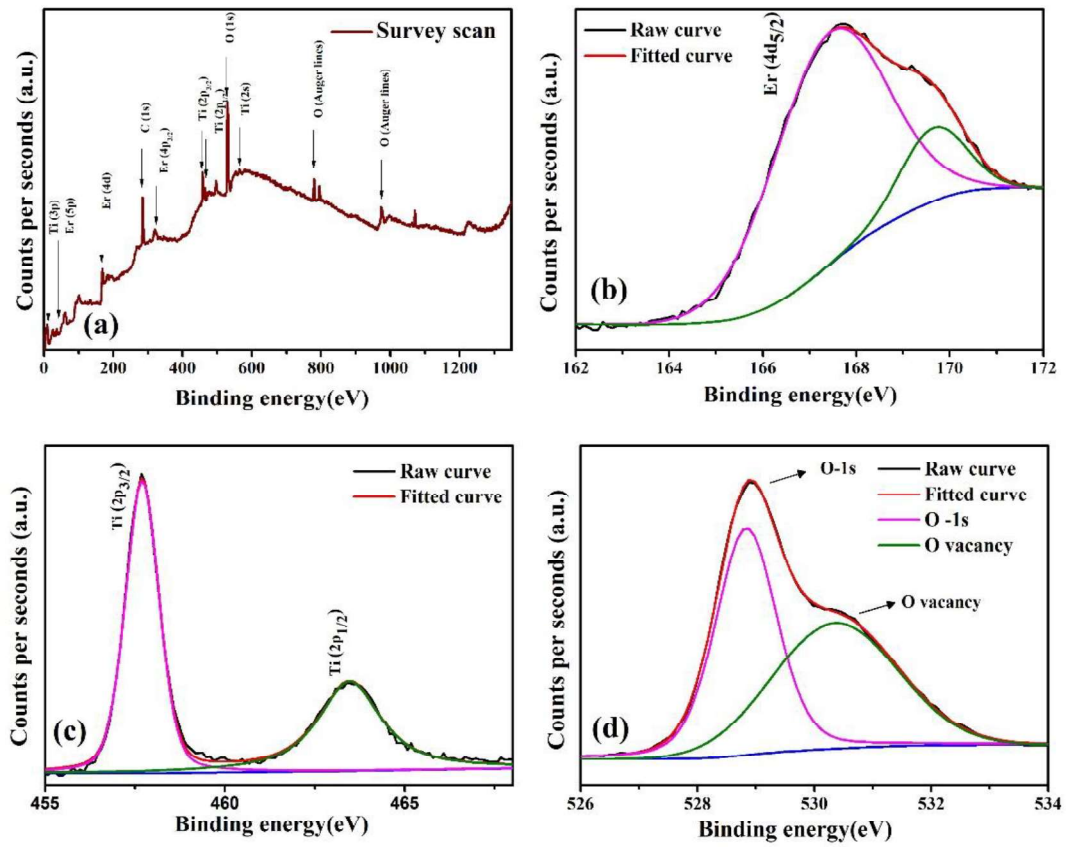


**Figure 6.5 x-ray photoelectron spectroscopy (XPS) (a) survey scan for $Er_2Ti_2O_7$ and core level XPS spectra for its constituent elements (b) Er-4d, (c) Ti-2p, and (d) O-1s state**

Further O-1s spectra in $Er_2Ti_2O_7$ have two peaks: one at a binding energy of 530.4 eV and another at 528.8 eV. The peak intensity at 530.4 eV decreases with Mn inclusion, which could be attributed to a change in the local electronic structure around oxygen atoms caused by the presence of Mn ions, resulting in a different hybridization between oxygen and metal atoms. These two peak structures are attributed to lattice oxygen at lower binding energies and to surface or defect-related oxygen at higher binding energies. The peak at 528.8 eV corresponds to the oxygen present at the lattice site denoted by $O_L$, and that at 530.4 eV corresponds to the

oxygen ($O_C$) that is chemisorbed from the surface or due to the creation of oxygen vacancies [132], [133].

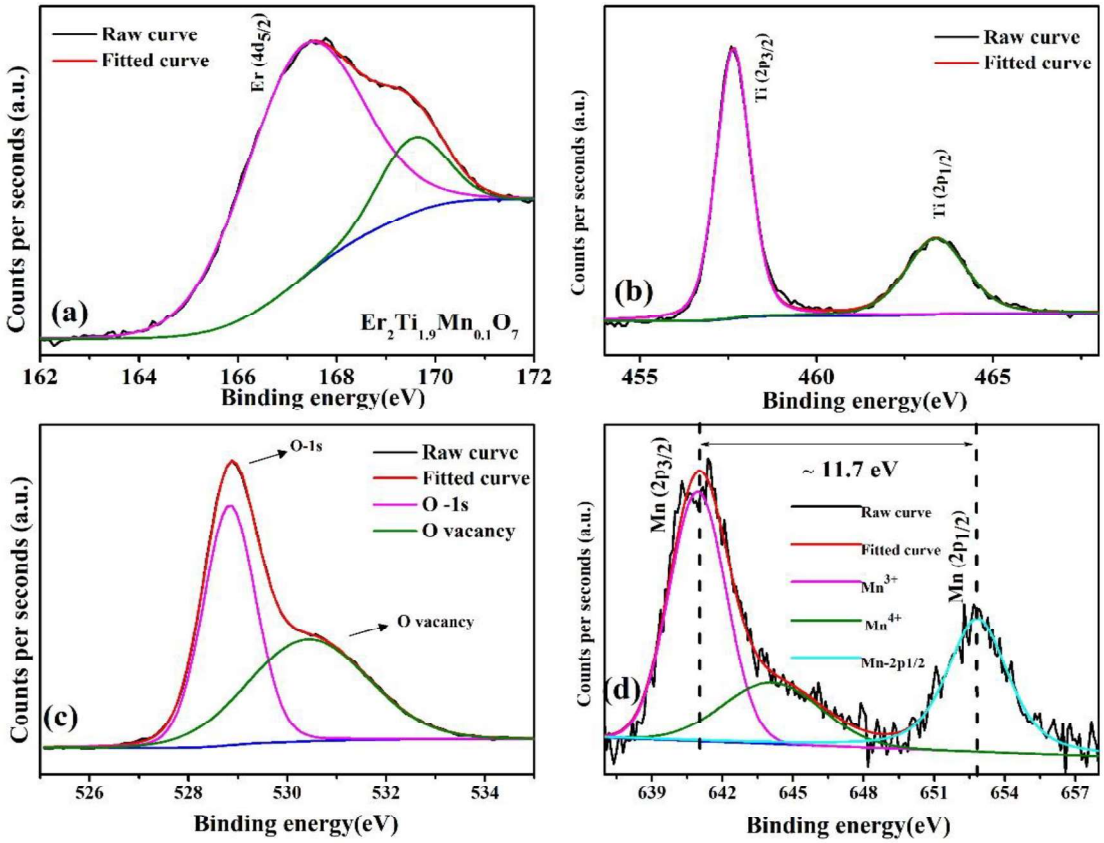


**Figure 6.6 ray photoelectron spectroscopy (XPS) of core level electronic states for constituent elements of $Er_2Ti_{1.9}Mn_{0.1}O_7$ (a) Er-4d, (b) Ti-2p, (c) O-1s, (d) Mn-2p.**

The high-resolution Ti-2p spectrum displays binding energies of 457.6 and 463.4 eV, which indicate the $Ti2p_{3/2}$ and $Ti2p_{1/2}$, respectively, typical for the $Ti^{4+}$ species [151]. The measured binding energy for Ti $2p_{3/2}$ peak is around 457.6 eV, which is in good agreement with the reference $Ti^{4+}$ systems. Although titanium can easily lower its valency, the spectra show no sign of $Ti^{3+}$ (455 eV) present in any of the compositions.

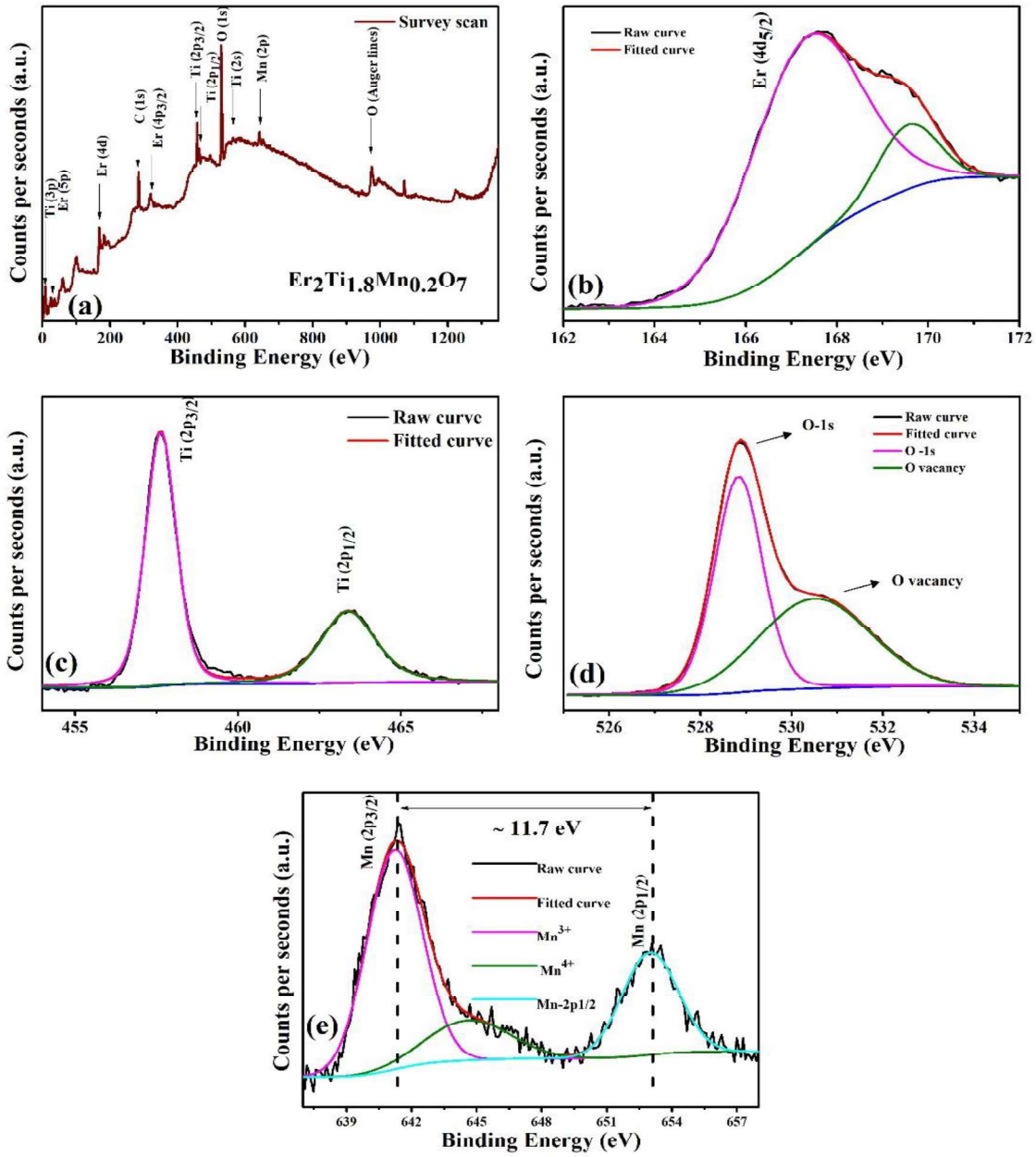


**Figure 6.7 x-ray photoelectron spectroscopy (XPS) (a) survey scan for $Er_2Ti_{1.8}Mn_{0.20}O_7$ and core level XPS spectra for its constituent elements (b) Er-4d, (c) Ti-2p, (d) O-1s, (e) Mn-2p.**

The observed fine structure of $Er^{3+}$ can be attributed to the hybridization of Er ions into Er—O, Er—Er and Er—Ti bonds and surface contamination [152]. In the two sets of spectra, each

fitting peak is assumed to follow the general shape of the Lorentzian-Gaussian function: one peak represents the Er-O bonds (located at 167.5 eV) and the second the Er-O-Ti bonds (located at 169.9 eV). The ionic state of Mn plays an important role in the lattice distortion. To check the manganese ionic state, the Mn–2p peak has been analyzed by XPS. In the high-resolution Mn 2p region, two peaks around 639.78 eV and 651.48 eV were observed, and their splitting width is 11.7 eV, which were ascribed to Mn $2p_{3/2}$ and Mn $2p_{1/2}$ [153]–[155]. The origin of these peaks is attributed to the spin-orbital coupling between the unpaired core 2p electron and the valence 3d electron. The wide and unsymmetrical nature of the $Mn2p_{3/2}$ peak further indicates the presence of multiple Mn valence states. The spin–orbit splitting between $Mn2p_{3/2}$ and $Mn2p_{1/2}$ was ~ 11.7 eV for both $Er_2Ti_{2-x}Mn_xO_7$ (x = 0.1 and 0.2) samples (**Figure 6.6 (d) and Figure 6.7 (e)**). The Mn 2p spectrum shows the coexistence of two oxidation states of Mn, namely $Mn^{3+}$ and $Mn^{4+}$ [156]. The absence of any satellite peak confirms that there are no $Mn^{2+}$ ions in the given systems.

## 6.2 Optical Studies on $Er_2Ti_{2-x}Mn_xO_7$ System

This section presents the study of the optical properties of the $Er_2Ti_{2-x}Mn_xO_7$ system through ultraviolet-visible and photoluminescence spectroscopy. The same has been discussed in sections 6.2.1 and 6.2.2, respectively.

### 6.2.1 Ultraviolet-visible spectroscopy

**Figure 6.8** depicts the room temperature UV-Vis absorption spectra for the $Er_2Ti_{2-x}Mn_xO_7$ system, recorded in the 200-1400 nm range. $Er_2Ti_2O_7$ consists of various narrow and well-resolved absorption bands present at 211, 303, 378, 405, 449, 486, 519, 648, 790 and 968 nm. Ligand-to-metal charge transfer (LMCT) phenomenon is responsible for the absorption peaks

at 211 nm and 303 nm corresponding to the transition from O-2p orbital of the valence band to the Ti-4d and Ti-3d state, respectively, of the conduction band. Other prominent absorption states of $Er_2Ti_2O_7$ present at 378, 405, 449, and 486 nm are also related to LMCT from O-2p to Ti states. For x = 0.1, i.e., with Mn inclusion at Ti site, the absorption peak at 303 nm is red-shifted to 350 nm. Mn exhibits an oxidation state of +4 in $Er_2Ti_{2-x}Mn_xO_7$, because it is substituted for $Ti^{4+}$ at the octahedral site. A large energy gap is created between unoccupied $e_g$ orbital and occupied $t_{2g}$ orbital of $Ti^{4+}$ because of the octahedral nature of the crystal electric field. With Mn inclusion, $t_{2g}$ state is shifted towards lower energy, thereby shifting the $Ti^{4+}$-3d state towards higher wavelength side. Additionally, in $Er_2Ti_{2-x}Mn_xO_7$ (x = 0.1 and 0.2), along with the absorption states of Ti at 211 and 350 nm, a dominant absorption state of $Mn^{4+}$ appears at 503 nm. It indicates LMCT from the O-2p to Mn-3d state. The rest of the higher wavelength LMCT absorption peaks from O-2p to Ti states is suppressed due to addition of Mn at Ti site in the $Er_2Ti_2O_7$ matrix. Bands present on higher wavelength sides are attributed to the f-f transitions within the $Er^{3+}$ states. Transitions related to higher wavelength regions between 500-1400 nm are associated to charge transfer transition (CTT), which is attributed to the inner transition confined within the 4f shells of $Er^{3+}$ ion. The electronic ground state of the free ion $Er^{3+}$ is $^4I_{15/2}$, resulting in sixteen (2S+1; 15/2+1 = 16) different vibrational states. The absorption peaks of $Er^{3+}$ ion centered at 519, 648, 790 and 968 nm are due to CTT and are identified as absorption from $^4I_{15/2}$ (ground state) to $^2H_{11/2,}$ $^4F_{9/2}$, $^4I_{9/2}$, and $^4I_{11/2}$ excited states respectively of $Er^{3+}$ as shown in the inset of **Figure 6.8** [138].

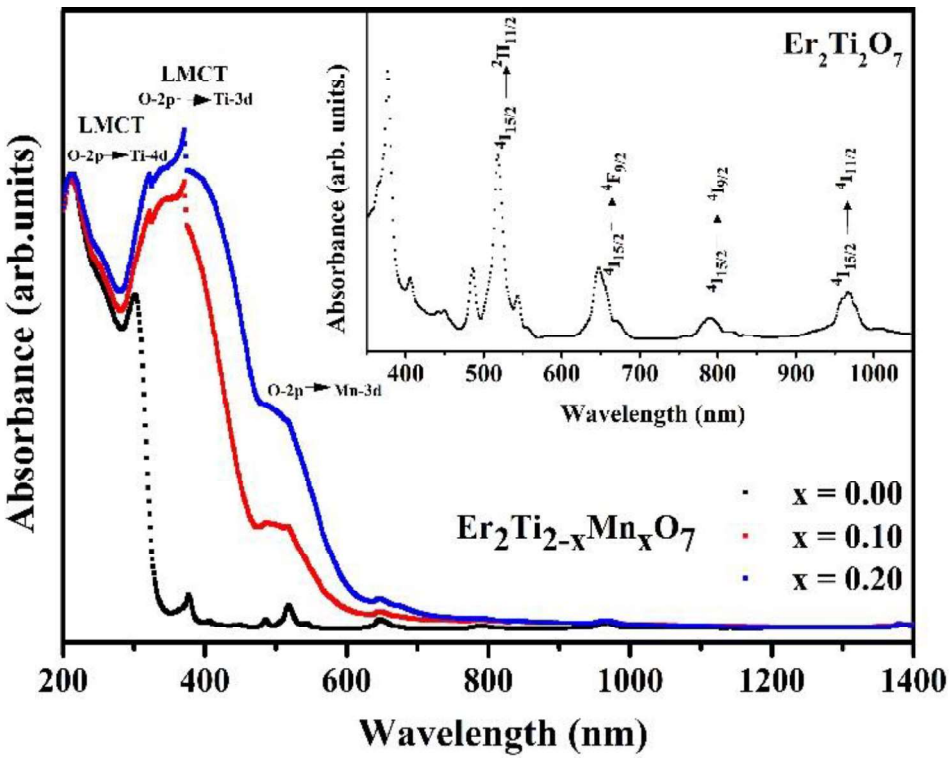


**Figure 6.8 Room temperature ultraviolet-visible (UV-vis) absorption spectrum of polycrystalline $Er_2Ti_{2-x}Mn_xO_7$ (x = 0, x = 0.10, and x = 0.20) compound in 200–1400 nm wavelength range. Inset shows the UV–vis spectrum of $Er_2Ti_2O_7$ in 700–1400 nm wavelength range.**

Further, band gap ($E_g$) has been determined from the absorption spectra of the $Er_2Ti_{2-x}Mn_xO_7$ system. Tauc equation; $\alpha h\nu = A\,(h\nu - E_g)$, where ν is the frequency of the incident photon, A denotes constant and is related to the type of materials, $E_g$ is the band transition energy, α indicates the absorption coefficient, n decides the type of transition, and it depends upon the material (n = 2 for direct and n = ½ for indirect electronic transition) is used for the same [157]. Tauc equation was plotted for the allowed direct transition, and the value of the intercept that denotes $E_g$ was taken from the extrapolation on photon energy axis till 0 eV from the linearly fitted graph between $(\alpha h\nu)^2$ versus hν, shown in **Figure 6.9.**

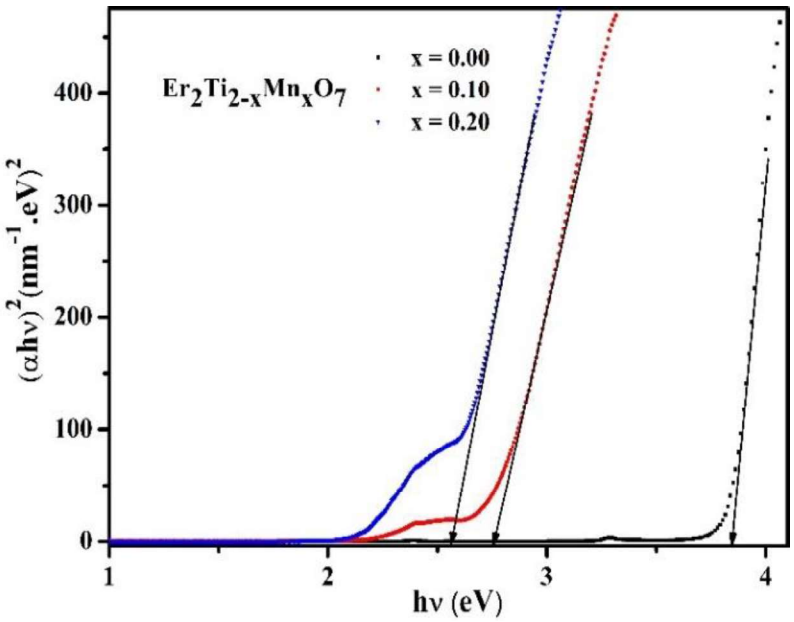


**Figure 6.9 $(\alpha h\nu)^2$ versus hν with linear fits for $Er_2Ti_{2-x}Mn_xO_7$ (x = 0, x = 0.10, and x = 0.20).**

The obtained value of bandgap ($E_g$) is 3.84 eV for $Er_2Ti_2O_7$ as obtained from the Tauc equation, which is in correspondence to the absorption peak at 303 nm (1240/303 = 4.1 eV). This is in correspondence to the electronic transition between $O^{2-}$-2p orbital and $Ti^{3+}$-3d orbital. $E_g$ decreases to 2.76 eV and further to 2.57 eV for x = 0.1 and x = 0.2, respectively, and the bandgap for $Er_2Ti_{2-x}Mn_xO_7$ is given in **Table 6.1.** Immediate decrease in bandgap to 2.76 eV for x = 0.1 is because of the emergence of new Mn state at 503 nm (1240/503 = 2.46 eV) that corresponds to LMCT from O-2p to Mn-3d state. Further increase in the concentration of Mn leads to the sequent reduction in bandgap from 2.76 to 2.57 eV due to the decrease in lattice parameter with rise in Mn percentage. Ti/Mn-O separation decreases from 2.182 Å for x = 0 to 2.180 Å for x = 0.2, as shown in **Table 6.1**. It results in the decrease in the splitting between orbitals contributing to conduction ($Mn^{4+}$) and valence band ($O^{2-}$) due

to decrease in the extent of hybridization. Hence, an entirely dissimilar electronic configuration of $Mn^{4+}$ relative to $Ti^{4+}$ results in the distortion of local crystal field in the vicinity of the $Mn^{4+}$ ion. Lattice distortion changes the orientation and Mn-3d orbital's energy levels which modifies the hybridization between Mn-3d and O-2p orbitals. This Mn inclusion at Ti site in $Er_2Ti_{2-x}Mn_xO_7$ manifests the optical band gap tenability. The band gap obtained experimentally are in good agreement with the theoretical result.

**Table 6.1 Band gap energies of $Er_2Ti_{2-x}Mn_xO_7$ (x = 0, 0.10 and 0.20) obtained from both experimental (through Tauc plot using UV-isible absorption spectra data) and theoretical data (DFT calculations).**

| Compound $Er_2Ti_{2-x}Mn_xO_7$ | Band gap (eV); experimental | Band gap (eV); theoretical | |
|---|---|---|---|
| | | LDA | LDA-1/2 |
| **x = 0** | 3.84 | 2.90 | 4.06 |
| **x = 0.10** | 2.76 | 2.05 | 2.52 |
| **x = 0.20** | 2.57 | 1.85 | 2.41 |

### 6.2.2 Photoluminescence spectroscopy

In addition to absorption spectra, we also obtained the emission spectra of the sample series to confirm the electronic energy levels for these compositions. Since the emission spectrum depends strongly upon excitation wavelength, the same was obtained for both 280 nm and 455 nm. Photoluminescence (PL) emission spectra were obtained with an excitation wavelength of 280 nm. $Er_2Ti_2O_7$ exhibits emission peaks at 341,396, 413, 421, 437, 450, 468, 481 and 493 nm. These emission peaks correspond to $Ti^{3+}$ and $O^{2-}$ transition. All the emission peaks get suppressed with Mn inclusion, as shown in **Figure 6.10**. Suppression is due to the emergence of a new absorption state of $Mn^{4+}$ in $Er_2Ti_{2-x}Mn_xO_7$ (x= 0.1 and 0.2). Emission now occurs due to cross-relaxation from $Mn^{4+}$ excited at 503 nm to the $Er^{3+}$ excited states and

finally CTT to the ground state of $Er^{3+}$. This explains the PL spectroscopy for the $Er_2Ti_{2-x}Mn_xO_7$ system. The electrons from both the Ti (303 nm) and Mn (503 nm) excited states relax to the excited state of $Er^{3+}$ through energy transfer and then relax to the ground state through emission. The emission intensity varies with the change in the extent of hybridization between Mn and its ligand atom.

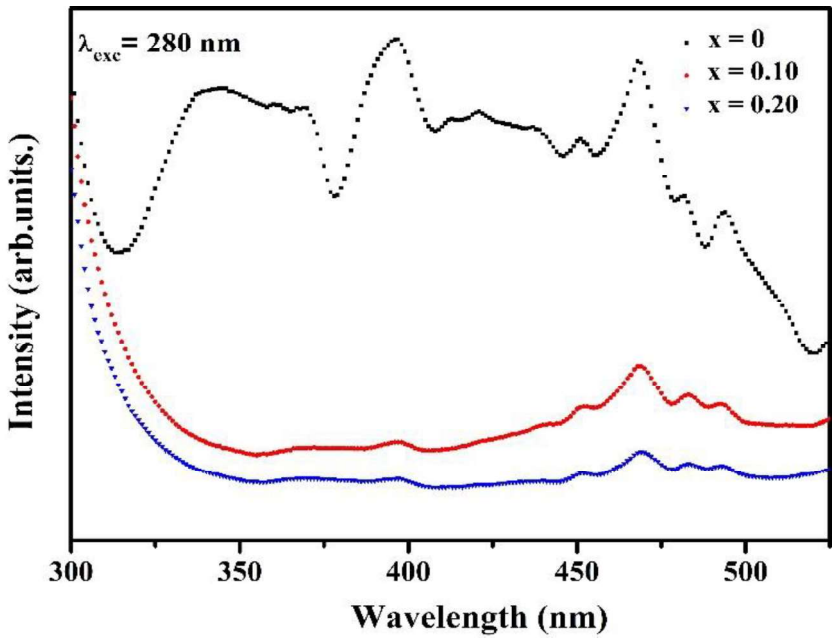


**Figure 6.10 Dependence of room temperature Photoluminescence (PL) emission spectra of $Er_2Ti_{2-x}Mn_xO_7$ (x=0, 1.10 and 0.20) using an excitation wavelength of 280 nm.**

Using an excitation wavelength of 455 nm, the luminescence spectra involve internal CTT within Er-4f states at 636 nm ($^7F_{9/2}$ ($D_5$) → $^4I_{15/2}$), 684 nm ($^7F_{9/2}$ ($D_1$) → $^4I_{15/2}$), 732 nm ($^4I_{9/2}$ ($B_5$) → $^4I_{15/2}$), 772 nm ($^4I_{9/2}$ ($B_5$) → $^4I_{15/2}$) and 826 nm ($^4I_{9/2}$ ($B_1$) → $^4I_{15/2}$) through a charge transfer transition phenomenon since the spectra do not exhibit any modification with Mn inclusion as shown in **Figure 6.11** [138].

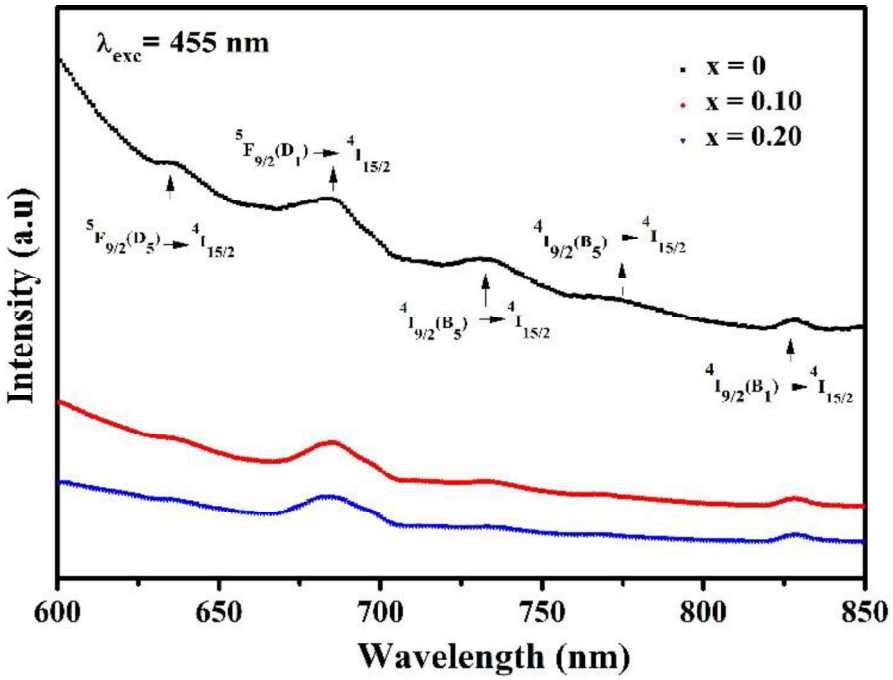


**Figure 6.11 Dependence of room temperature photoluminescence (PL) emission spectra of $Er_2Ti_{2-x}Mn_xO_7$ using an excitation wavelength of 455 nm.**

As discussed above, the possible mechanism and the energy level diagram involving the absorption and emission from the $Er^{3+}$, $Mn^{4+}$, $Ti^{4+}$ and $O^{2-}$ states are schematically shown in **Figure 6.12.**

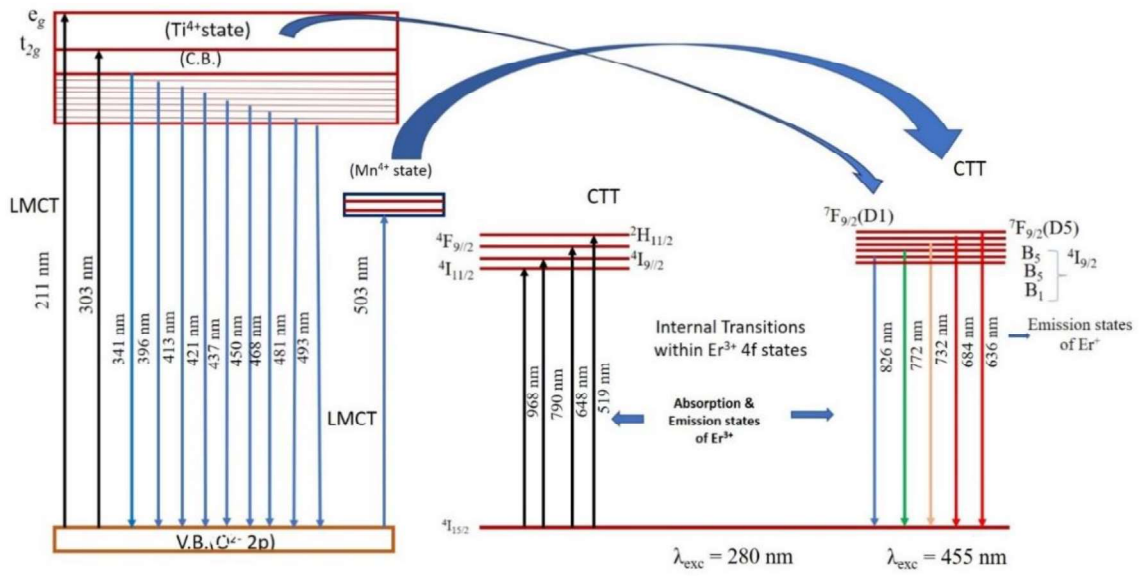


**Figure 6.12 Mechanism and the energy level diagram involving the absorption and emission from the $Er^{3+}$, $Mn^{4+}$, $Ti^{4+}$ and O2- states in $Er_2Ti_{2-x}Mn_xO_7$**

## 6.3 Conclusions

This chapter presents optical spectroscopy and electronic structure calculation of $Mn^{4+}$ doped pyrochlore, $Er_2Ti_2O_7$. It has been established that perturbation changes the electronic structure in such spin-disordered systems. The band gap calculated using a theoretical approach (density functional theory calculations) matches well with the experimental band gap value obtained using a Tauc plot in U.V. Visible absorption spectroscopy. The Raman spectroscopy shows the variation in peak intensity and peak width. The variations in peak intensity of the Raman spectrum can be attributed to alterations in the local crystal field and symmetry of the system caused by the Mn substitution. In the high-resolution Mn 2p region of XPS, two peaks around 639.78 eV and 651.48 eV were observed, and their splitting width is 11.7 eV, which

were ascribed to Mn $2p_{3/2}$ and Mn $2p_{1/2}$. The origin of these peaks is attributed to the spin-orbital coupling between the unpaired core 2p electron and the valence 3d electron. The Mn 2p spectrum shows the coexistence of two oxidation states of Mn, namely $Mn^{3+}$ and $Mn^{4+}$. The UV-vis spectra show that with immediate Mn inclusion at the Ti site, the absorption peak of $Ti^{4+}$ at 303 nm shifts to 350 nm. An increase in the percentage inclusion of Mn in $Er_2Ti_{2-x}Mn_xO_7$ results in a sequential reduction in bandgap from 3.84 eV (x = 0) to 2.76 eV (x = 0.1) and subsequently 2.57 eV (for x = 0.2). This is attributed to the reduction in lattice parameter with the increase in Mn concentration. It establishes the optical band gap tunability through Mn inclusion at Ti site in $Er_2Ti_{2-x}Mn_xO_7$. The subsequent insulator-semiconductor transition tenability can be explored in sensing applications. These wide bandgap semiconductors tuning electronic properties between conventional semiconductors and insulators and can be further exploited in various material applications in devices where precise wavelengths are required. The next chapter summarizes the entire thesis work and lists a few suggestions regarding the future scope of this work.